Studies of nuclear equation of state with the HIRFL-CSR external-target experiment

Dong Guo,[1] Xionghong He,[2] Pengcheng Li,[3] Zhi Qin,[1] Chenlu Hu,[2] Botan Wang,[4] Yingjie Zhou,[5]
Yapeng Zhang,[2] Xianglun Wei,[2] Herun Yang,[2] Dongdong Hu,[5] Ming Shao,[5] Limin Duan,[2]
Yuhong Yu,[2] Zhiyu Sun,[2] Yongjia Wang,[3] Qingfeng Li,[2,3] Kun Zheng,[1] and Zhigang Xiao[1,*]

[1]*Department of Physics, Tsinghua University, Beijing 100084, China*
[2]*Institute of Modern Physics, Chinese Academy of Science, Lanzhou 730000, China*
[3]*School of Science, Huzhou University, Huzhou 313000, China*
[4]*Department of Engineering Physics, Tsinghua University, Beijing 100084, China*
[5]*Department of Modern Physics, University of Science and Technology of China, Hefei 230026, China*

The HIRFL-CSR external-target experiment (CEE) under construction is expected to provide
novel opportunities to the studies of the thermodynamic properties, namely the equation of state of
nuclear matter (nEOS) with heavy ion collisions at a few hundreds MeV/u beam energies. Based
on Geant 4 packages, the fast simulations of the detector responses to the collision events generated
using transport model are conducted. The overall performance of CEE, including spatial resolution
of hits, momentum resolution of tracks and particle identification ability has been investigated.
Various observables proposed to probe the nEOS, such as the production of light clusters, $t/^3$He
yield ratio, the radial flow, π^-/π^+ yield ratio and the neutral kaon yields, have been reconstructed.
The feasibility of studying nEOS beyond the saturation density via the aforementioned observables
to be measured with CEE has been demonstrated.

I. INTRODUCTION

The phase diagram of nuclear matter is of significance
in understanding the properties of the strong interaction
described by Quantum Chromodynamics (QCD) and the
evolution of the universe. With the relativistic heavy ion
experiments, the various experimental signals have re-
vealed that strongly interacting matter may undergo the
transition from the hadron phase to the quark-gluon-
plasma (QGP) phase, for which the transition at low
baryon density and high temperature is crossover [1–3].
Fig.1 shows the QCD phase diagram of current under-
standing [4]. Despite of great progress along this di-
rection, a few important questions remain unsolved con-
cerning the QCD phase diagram. For instance, what are
the thermodynamic properties of QCD and where is the
phase boundary between QGP and hadronic matter at
high net-baryon density? Does the critical end point
(CEP) exist and where is the location? To shed light
on these questions, it is of great significance to explore
further the QCD phase diagram with more systematic
studies.

Relativistic heavy ion collisions (HIC) over wide en-
ergy range provide the unique way to study QCD phase
diagram in terrestrial laboratory. Over the past two
decades, nuclear collisions at the Relativistic Heavy Ion
Collider (RHIC) and the Large Hadron Collider (LHC)
have collected a large amount of data searching for first-
order phase transition signals and precise phase transi-
tion CEP. Between 2010 and 2017, RHIC completed the
first phase of the beam energy scanning program (BES-
I) [5, 6]. The second phase (BES-II) was launched in
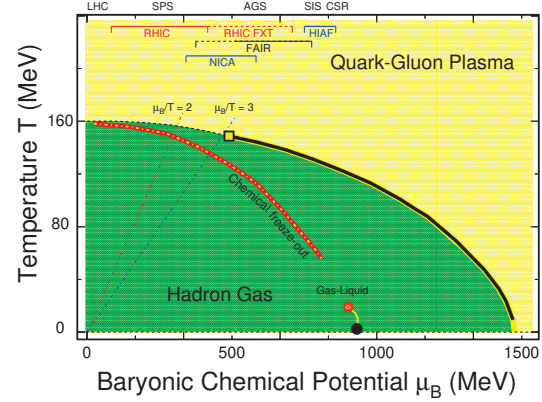2018, focusing on the collisions with $\sqrt{S} \leq 27$ GeV to

FIG. 1. (Color online) QCD phase structure diagram of
temperature and baryon chemical potential description [4].
The red line in the figure is the chemical freeze-out curve of
common nuclear substances obtained by experiments. The
black square points and black solid lines represent the ex-
pected first-order phase boundaries and critical points. The
red circle represents the CEP at which the nuclear material
becomes gas-liquid phase. The study areas of RHIC beam en-
ergy scanning and fixed target (USA), NICA (Russia), FAIR
(Germany), and HIAF (China) are shown at the top of the
figure.

search sensitive observable of QCD phase transitions [7–
9], including net proton [4, 10–13], net charge [14], net
Kaon multiplicity distribution and high order moment
analysis [15]. Fig.2 shows the energy dependence of net
proton high momentum $\kappa\sigma^2$ in Au+Au collisions with
the centrality of $0-5\%$ collected in RHIC BES-I [4]. It
is observed that $\kappa\sigma^2$ of net proton is closely related to
that of proton and exhibits a non-monotonic dependence
on collision energy with a significance of 3.1σ [11, 13].
In addition, the prediction of UrQMD calculation, which

* xiaozg@mail.tsinghua.edu.cn

incorporates conservation laws and most of the relevant physics apart from a phase transition and mean field potentials, does not coincide with the trend of the data points at low energies, which means that accurate measurement is very important in the supra-saturation density region and lower beam energies to further reduce experimental errors. In addition to the existing ones, many more experiments are in schedule, like CBM at FAIR, MPD at NICA etc.
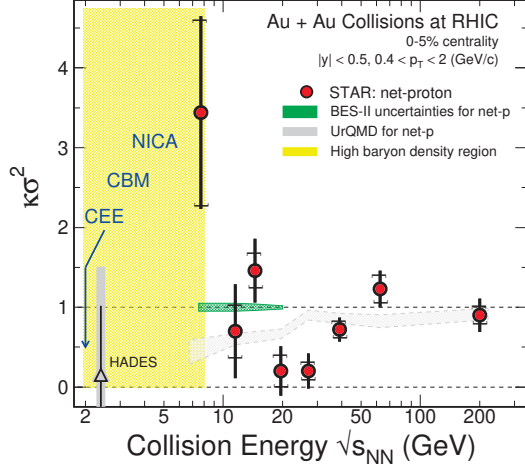

FIG. 2. (Color online) Energy dependence of net proton and proton $\kappa\sigma^2$ in Au+Au collisions at the center $(0-5\%)$ of RHIC BES-1 [4]. The results of the HRG and UrQMD models are shown as dotted lines and gold bands, respectively.

In hadron phase, the key component of the QCD phase structure is the equation of state of nucleonic matter (nEOS) [16]. For the convenient definition of nEOS, one writes the nucleon specific energy $E(\rho, \delta)$ of nucleonic matter at zero temperature in quadratic form

$$E(\rho, \delta) = E_0(\rho) + E_{\text{sym}}(\rho)\delta^2 \tag{1}$$

where $\delta = (\rho_n - \rho_p)/(\rho_n + \rho_p)$ is the isospin asymmetry, ρ_n and ρ_p are the density of neutrons and protons. $E_0(\rho)$ is the nucleon specific energy in symmetric nuclear matter and $E_{\text{sym}}(\rho)$ is the density dependent nuclear symmetry energy. Keeping the lowest order terms, for the symmetric nuclear matter, the nEOS can be written in

$$E_0(\rho) = E_0(\rho_0) + \frac{\kappa_0}{2}\left(\frac{\rho - \rho_0}{3\rho_0}\right)^2 + \frac{J_0}{6}\left(\frac{\rho - \rho_0}{3\rho_0}\right)^3 + \frac{Z_0}{24}\left(\frac{\rho - \rho_0}{3\rho_0}\right)^4, \tag{2}$$

where the coefficients κ_0, J_0 and Z_0 are the incompressibility, skewness and kurtosis parameters, respectively.

The nuclear symmetry energy is expressed as

$$E_{\text{sym}}(\rho) = E_{\text{sym}}(\rho_0) + L\left(\frac{\rho - \rho_0}{3\rho_0}\right) + \frac{K_{\text{sym}}}{2}\left(\frac{\rho - \rho_0}{3\rho_0}\right)^2, \tag{3}$$

where L and K_{sym} are the slope and curvature parameters of the nuclear symmetry energy at normal nuclear matter density ρ_0, respectively.

In HIC from a few hundred MeV/u to a few GeV/u, nuclear matter above saturation density is created. The density gradients of the compressed nuclear matter will be developed to various forms of flow carrying the information of nEOS, and in return, the flow has been used to probe the incompressibility of nuclear matter [17]. Recently, HADES collaboration has published the proton triangular flow v_3 data at 2.4 GeV. Compared to UrQMD transport model calculations, it is shown that the proton v_3 exhibits high sensitivity to the hadron medium EoS [18]. In addition to the flow analysis, the production of K meson, particularly near threshold, is sensitive to the density of the compressed participant region, and thus is employed as a probe of nEOS. Thanks to the great efforts from the communities of nuclear physics and astrophysics, the knowledge of $E_0(\rho)$ from ρ_0 to a few times of ρ_0 is accumulated.

The least known term of nEOS is the density behavior of symmetry energy $E_{\text{sym}}(\rho)$. Since the $E_{\text{sym}}(\rho)$ gives rise to the isospin diffusion and isospin drift mechanisms, in the terrestrial laboratory, HIC involving neutron rich nuclei provide unique opportunities to constrain $E_{\text{sym}}(\rho)$ near and above the saturation density. In a wide energy range, various isospin probes have been identified and applied to constrain $E_{\text{sym}}(\rho)$ near and above ρ_0 in the last two decades [19–26]. Some new probes are also introduced or updated very recently, including the neutron skin thickness of heavy nuclei [27, 28], the angular distribution of average N/Z of light charged particles [29], anticorrelation of the $t/^3$He yield ratio with the heavy clusters [30] for $\rho \approx \rho_0$ and the π^-/π^+ ratio for $\rho > \rho_0$ [31]. Moreover, since the observation of the neutron star merging event GW170817, great progress has been made to constrain $E_{\text{sym}}(\rho)$ by combining the GW170817 and heavy ion data [32, 33]. For a recent review, one can refer to [34].
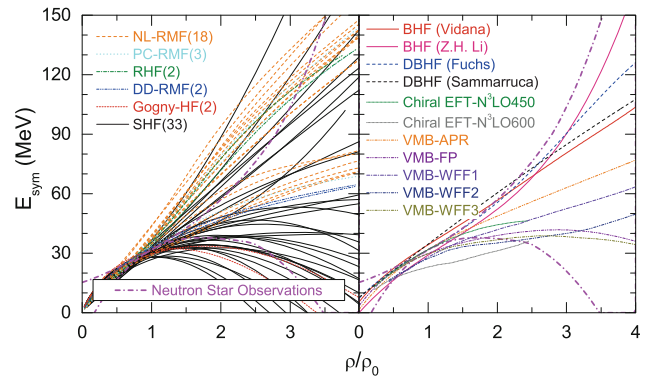

FIG. 3. (Color online) Research the constraints of symmetry energy in the supra-saturation density region from various theories, and display the constraints on the boundary through neutron star data [35]

Despite of great progress achieved in the last two decades, still the constraint of $E_{\text{sym}}(\rho)$ suffers from large uncertainties [33, 36–39], particularly at high density region. World wide efforts in this direction is still on-going. In order to finally determine $E_{\text{sym}}(\rho)$ in the supra-saturation density region, some new experiments are scheduled or have conducted at some large scientific devices in the world, including but not limited to HADES at GSI, SπRIT at RIKEN, RAON-LAMPS in Korea etc. These latest experiments will certainly provide better experimental conditions and improve the statistics and reduce the uncertainties. For the recent review, one can refer to the long report [40].

To this end, in addition to the RHIC-STAR energy scan experiment, there are several large experimental facilities in operation or construction around the world, which are of great significance for mapping the QCD phase diagrams at high net baryon number density, as well as for constraining the nEOS in hadron phase. In addition to the aforementioned facilities around the world, CEE is currently under construction at the T_4 Experimental Terminal of the Heavy Ion Research Facility (HIRFL) in Lanzhou [41, 42], aiming at collecting the first physics data by 2025. The High Intensity Heavy Ion Accelerator Facility (HIAF) is under construction in Huizhou, China [43]. The HIAF in design will be able to provide beams of whole ion species, with the highest center of mass energy in U+U collisions being $\sqrt{S_{NN}} = 4$ GeV. The upgraded CEE$^+$ will be placed in terminal T2 of the HIAF for high energy experiments, providing great opportunities in the studies of QCD phase structure in high baryon density region and EoS of nuclear matter in high density.

In this paper, the design, performance and feasibility of various physical goals related to the EOS studies with CEE are introduced. The simulations are carried out in the framework of Geant 4. The ultra-relativistic quantum molecular dynamics (UrQMD) model which incorporates the Skyrme potential energy density functional and the in-medium nucleon-nucleon cross section is adopted as the event generator [44–46]. The analysis and reconstructions of the simulated data are done in CEE-ROOT platform, which is developed by the collaboration of the CEE experiment, inheriting from Fair ROOT [47]. The paper is arranged as following. Section II presents the structure of CEE in the technique design and the main functions of each detector subsystem. Section III introduce the expected performance of CEE, including the spatial acceptance, momentum resolution, PID ability, and the construction of CEE global trigger signal. Section IV presents the verification of a few probes sensitive to the EOS of nuclear matter beyond saturation density, including the yield of light clusters, radial flow, π^-/π^+ ratio and yield of neutral Kaon mesons. Section V presents a summary.

II. STRUCTURE AND SIMULATION OF CEE

A. Structure of CEE

Aiming at the studies of the EOS of nuclear matter at approximately $2\rho_0$, where ρ_0 is the saturation density, CEE is designed to measure the charged particles in nearly 4π space in center of mass reference [41]. The design of the CEE is shown in Fig.4. The main component of CEE is a large-gap dipole magnet, housing the tracking detectors in a nearly homogeneous field of 0.5 T along the vertical direction. The target is located inside the field, so that the tracking detectors can cover large solid angle. The tracking detectors include two time projection chambers (TPC) [48] surrounded by the inner time-of-flight (iTOF) detectors covering the midrapidity [49], and an array consisting of three multiwire drift chambers (MWDC) followed by an end cap time-of-flight (eTOF) wall for the measurement of charged particles at forward rapidity [50]. At the downstream end of the CEE spectrometer, there is an array of plastic scintillators to measure the charged particles near zero degree (ZDC) [51]. The start timing detector (T_0) [52, 53] and the active collimator (AC) are placed on the beam line in the upstream side of the target. Besides, there is also a silicon pixel positioning detector (SiPix) [54, 55] to monitor the beam position at the upstream side to T_0. Tab.I shows the main technical performance of CEE system.
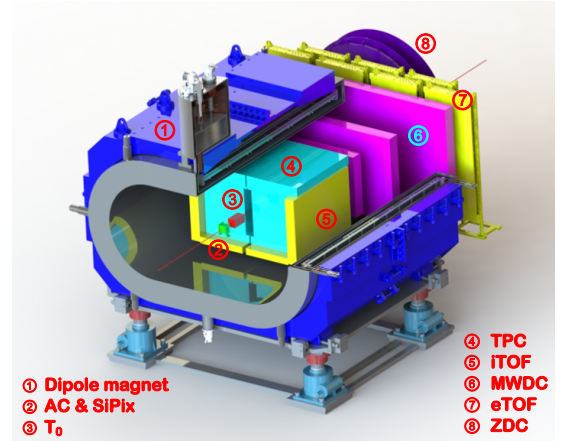

① Dipole magnet ④ TPC
② AC & SiPix ⑤ iTOF
③ T$_0$ ⑥ MWDC
  ⑦ eTOF
  ⑧ ZDC

FIG. 4. (Color online) The design of the CEE

TABLE I. (Color online) Technical indicators of CEE.

Item	value
Maximum beam energy	$0.5\text{GeV/u(U)} - 2.8\text{GeV(p)}$
Bean type	$p \sim U$
Maximum event rate	10 kHz
Acceptance	$> 50\%$
Total channel number	20k

The tracking detector at midrapidity are the two iden-

tical TPCs surrounded by iTOF walls. The two TPCs are installed in a left-right symmetric mode in order to leave the 20 cm space in between for the beam passing through. The target position is in the gap of the two TPCs, being 15 cm to the rear surface of the field cage. The electronics of the TPCs are placed on the top plane above the two TPCs. The high voltage is fed into the field cage from the bottom plane. A high voltage step-down structure surrounded by teflon blocks is designed to avoid a sharp voltage decrease near the HV point. The field cages are made of Kapton layer with copper electrodes printed on both surfaces, ensuring the distortion of the electric field to be less than 0.1%. A three-layer large-area gaseous electron multiplier (GEM) foils are stacked on the top of the sensitive volume of TPC to amplify the arrived electrons and then induce signals on the readout pads. The signals of each pad are readout by the specially designed front end electronics (FEE) and then transferred to the digitization board adopting SAMPA chips [56, 57].

The forward tracking detectors consist of three MWDCs and an eTOF wall placed at forward angle. Two sets of MWDC are placed inside the field of the dipole and the third one followed by the eTOF wall are placed outside the magnet. On each MWDC and the eTOF wall, an inactive area is designed for the beam particles to pass through without inducing enormous charges in the sensitive volume of the detectors. Each MWDC contains six layers of sensitive wires in three directions, called X, U and V wires, meeting $0°$, $30°$ and $-30°$ with respect to the vertical direction, respectively. For each direction of wire, there are two layers of drift cells, displacing by half size of a cell in order to discriminate the ghost hit. Both the entrance and exit windows of the MWDCs are made of aluminum coated Mylar foil. The detector operates in atmospheric flow-gas mode. The high voltage are fed to the anode wires directly. The signals, readout with a capacitance coupling, is amplified and shaped in the FEE before being transferred to a SCA chip for digitization. Then the digitized data are sent to the BDM module, where the timing and amplitude information is online computed and transferred to DAQ system for saving. Tab.II lists the main geometric dimensions and technical specifications of the TPC and MWDC.

The time-of-flight (TOF) signals are measured by T_0, inner TOF wall (iTOF) and the outer TOF wall (eTOF), respectively. The T_0 placed in front of the target is made of scintillator foil read out by SiPM from the side, delivering the initial time of heavy ion collision. Both iTOF and eTOF, consisting of multi-gap resistive plate chambers (MRPC), are installed to record the arrival time of the charged particles passing through TPC and MWDC, respectively. Thus, combining the tracking and TOF detectors, one can deduce the PID information via $dE/dx - p/Q$ in the tracking detectors and $p/Q - \beta$, respectively, where p is the momentum and β is the velocity calculated from the track length and TOF. Tab.III shows the main performances of TOF system. The total area of the iTOF and eTOF systems is about 12 m^2. In

iTOF and eTOF, the hitting position can also be derived through the time difference of the signals at both ends.

The iTOF, grouped by modules, surrounds the left, right and bottom surfaces of the TPC. The upper surface is not covered by TOF detectors because the readout electronics of the TPC is arranged on the top. The left and right iTOF walls are composed of six iTOF modules, each iTOF module contains three MRPC detectors, and the left and right envelope size is $100(x) \times 1000(y) \times 1355(z)$ mm^3. The bottom iTOF wall contains two symmetrical parts, consisting of 6 iTOF modules and 12 MRPC detectors, with the bottom envelope size of $670(x) \times 1355(z) \times 100(y)$ mm^3. The eTOF wall is located at the down stream end of the dipole magnet, being 2.6 m to the target position. Each MRPC has 10×0.25mm air gaps and self-sealing technology is applied for the first time. The whole wall is divided into 7 modules, each module contains $3 \sim 4$ self-sealed MRPC [50]. The signals of the TOF detectors are collected and amplified by the MRPC special electronics chip NINO [58] in FEE, and then the high precision time information is obtained through the high performance time digitization module (TDM) [59].
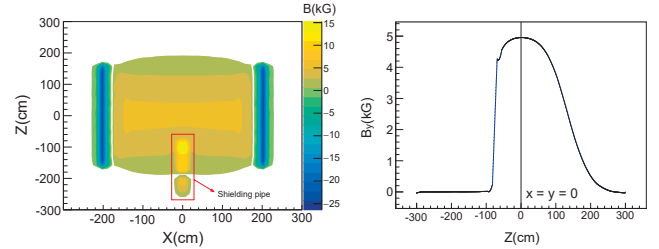

FIG. 5. (Color online) The magnetic field distribution in the center of the secondary magnet. The left (a) shows the magnetic field distribution in the X-Z plane, and the magnetic field shield tube is shown in the red box; The right figure (b) shows the distribution of magnetic field intensity in the y direction in the beam direction

The active collimator functioning to veto the off-target reaction background is placed between T_0 and the target. It is composed by four plastic scintillators (250×250 mm^2) distributed around the entrance of the target chamber, leaving a 50×50 mm^2 hole in the center. The SiPM is used to read out the signals.

The ZDC is mainly used to measure the spectators from HIC, and to determine the centrality and the reaction plane of collisions. The ZDC is located at the most downstream position of the whole spectrometer, about 300 cm to the target. The overall transverse layout of ZDC is rotationally symmetric to the beam line. It is divided into 24 equal sectors, each of which contains 8 trapezoid scintillators placed in row along the radial direction. The outer radius of the ZDC sensitive area is 100 cm while the inner radius is about 10 cm, through which the non-reacted beam particles can pass.

The large gap superconducting dipole magnet is to

TABLE II. (Color online) The geometry size and technical indicators of TPC and MWDC

TPC parameters		MWDC parameters	
Item	value	Item	value
Effective sensitive area (half)	$500(x) \times 800(y) \times 900(z)$ mm^3	MWDC1 effective sensitive area	$136(x) \times 63(y)$ cm^2
Channel number	≥ 10000	MWDC2 effective sensitive area	$190(x) \times 88(y)$ cm^2
Sensitive area of GEM film	900 mm $\times 500$ mm	MWDC3 effective sensitive area	$274(x) \times 126(y)$ cm^2
Track multiplicity	< 100	Channel number	≥ 3000
Maximum event rate	1kHz	Transverse position resolution	0.3 mm
Maximum field strength	400 V/cm	Track reconstruction efficiency	$\sim 98\%$
Momentum resolution	$\sim 5\%$	Momentum resolution	$\sim 5\%$

TABLE III. (Color online) The technical indicators of iTOF and eTOF

iTOF parameters		eTOF parameters	
Item	value	Item	value
Total effective area	6 m^2	Total effective area	3.2×1.6 m^2
Channel number	~ 2400	Channel number	~ 1500
Average count rate of single channel	10kHz	Average count rate of single channel	10kHz
Time resolution accuracy	< 50ps	Time resolution accuracy	< 60ps

bend the charged particles produced in the projectile-target collisions. The raw dimension of the magnet is $2700(L) \times 4300$ (W) $\times 2.7$ (H) mm^3. The space of the uniform field housing the sensitive volume of the TPC is 900 (L) $\times 1200$ (W) ~ 800 (H) mm^3. The central field is 0.5 T in strength with a uniformity better than 5%. Fig.5 shows the magnetic field distribution in the center of the dipole magnet.

In addition, the CEE also includes the following supporting systems. The data acquisition system (DAQ) uses D-Matrix architecture to provide data storage. The main function of the clock system is to provide high precision global synchronous clock for the electronics modules and DAQ system. The trigger system provides global trigger signals in beam experiments or in detector test run. Refer to Section III C for details about the construction of the global trigger signals of CEE.

B. Event generator and simulation tool

In order to constrain nEOS, particularly for supra-saturation density, one usually use the given $E_0(\rho)$ and $E_{\mathrm{sym}}(\rho)$ as input in transport model for HIC or in solving the Tolman–Oppenheimer–Volkoff (TOV) equations for neutron star structures. The predicted results are then compared to experimental data or astrophysical observations. By adjusting the parameters of $E_0(\rho)$ and $E_{\mathrm{sym}}(\rho)$ until the results converges to the experimental results, one arrives a constraint of nEOS. And in return, transport model is usually employed as the event generator in the feasibility studies of nEOS via in terrestrial heavy ion experiment.

UrQMD model is a transport model widely used to describe the relativistic heavy ion collisions and proton induced reaction process [60, 61], ranging from sub-GeV/u to TeV/u energies covered by SIS, AGS, SPS, RHIC and LHC. In order to apply the UrQMD model as an event generator for CEE, the model is adopted by improving the isospin-dependent nuclear potential and collision terms.

The UrQMD model as the event generator is operated and provided by Huzhou University in China [44–46], and the main improvements include: 1) The mean-field potential derived from the Skyrme potential energy density functional has been implemented into [46, 62, 63] 2) The nuclear medium effects on NN cross sections are considered, the density-, momentum- and isospin-dependent NN cross section is adopted [44, 64–66]; 3) The isospin-dependent minimum spanning tree (iso-MST) method [67] is adopted to construct clusters. In addition, the yield and flow observables about π and K, which are effective and sensitive probes of symmetry energy, can be better reproduced by introducing proper pion-nucleon potential and kaon-nucleon potential [33, 68, 69]. The effective two-body interaction potential energy U is decomposed into the Coulomb energy U_{Coul}, the Skyrme potential energy U_ρ and the momentum-dependent potential energy U_{md}. The U_ρ and U_{md} is written as $U_{\rho,\mathrm{md}} = \int u_{\rho,\mathrm{md}} \mathrm{d}\mathbf{r}$, where

$$u_\rho = \frac{\alpha}{2} \frac{\rho^2}{\rho_0} + \frac{\beta}{\eta+1} \frac{\rho^{\eta+1}}{\rho_0^\eta} + \frac{g_{\mathrm{sur}}}{2\rho_0} (\nabla \rho)^2 + \frac{g_{\mathrm{sur,iso}}}{2\rho_0} [\nabla(\rho_n - \rho_p)]^2 + u_\rho^{\mathrm{sym}},$$

(4)

and

$$u_{\mathrm{md}} = t_{\mathrm{md}} \ln^2 \left[1 + a_{\mathrm{md}}(\mathbf{p}_i - \mathbf{p}_j)^2\right] \frac{\rho}{\rho_0}.$$

(5)

The symmetry potential energy density functional reads as

$$u_\rho^{\mathrm{sym}} = \left[A_{\mathrm{sym}}(\frac{\rho}{\rho_0}) + B_{\mathrm{sym}}(\frac{\rho}{\rho_0})^\gamma + C_{\mathrm{sym}}(\frac{\rho}{\rho_0})^{5/3}\right]\delta^2\rho. \tag{6}$$

For the Skyrme interactions, the symmetry potential energy terms come from two-body, three-body interaction terms, and its related parameters are A_{sym}, B_{sym}, and C_{sym}, respectively. All the parameters used in the UrQMD model, such as α, β, η, g_{sur}, $g_{\mathrm{sur,iso}}$, A_{sym}, B_{sym}, C_{sym} can be derived from the standard Skyrme parameters, x_0, x_1, x_2, x_3, t_0, t_1, t_2, t_3, σ [62, 63, 70]. In addition, one can set $A_{\mathrm{sym}} = C_{\mathrm{sym}} = 0$ and $B_{\mathrm{sym}} = C_s/2$, and adopt the density power law form to investigate the density-dependent symmetry energy[70, 71]

$$u_\rho^{\mathrm{sym}} = \left[\frac{C_s}{2}(\frac{\rho}{\rho_0})^\gamma\right]\delta^2\rho. \tag{7}$$

The simulations and the reconstructions of CEE experiment is implemented in the framework called CEE-ROOT, a platform inheriting from Fair ROOT software [47] based on the ROOT and Geant 4 packages. User routines are developed to complete the data calibration, event reconstruction, efficiency correction and histograming. In CEEROOT, the subdetectors, the dipoles and the main materials are constructed using Geant 4 class libraries. When the particles produced in HIC provided by the event generator are input to the simulator, the propagation of the particles and the responses of the detectors are simulated. Then the signals in the sensitive volume of the detectors are digitized and saved to hard disk for further reconstruction. In this studies, the detector systems, including the magnetic field, T_0, iTOF, eTOF, TPC, MWDC and ZDC are constructed as designed. The improved UrQMD model described in Section.II A is used as the event generator. Fig.6 shows the event display and detector configuration in the simulations. The detector performance based on fast simulations will be introduced in the next section.
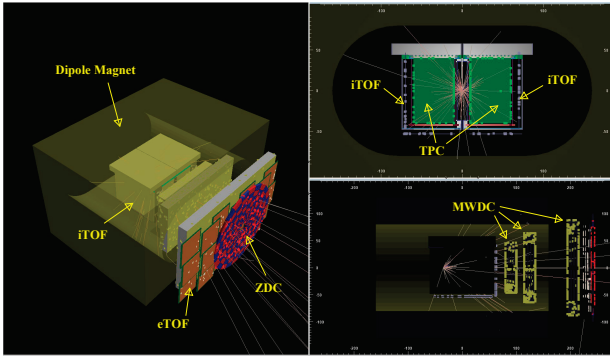

FIG. 6. (Color online) The detector structure and the event display of CEE in fast simulation.

III. CEE PERFORMANCE STUDY

This section presents the fast simulation studies on CEE performance. Using a symmetric collision ^{208}Pb+^{208}Pb, the acceptance, the PID ability and the centrality selectivity are discussed. The design of the global trigger design in heavy ion collision of CEE is introduced.

A. Acceptance

It is usually required to measure nearly the whole products in the studies of nuclear EOS and QCD phase structure, naturally one favors large acceptance for CEE. Fig.7 shows the phase space distribution of different kinds of particles at $b = 0$ fm in ^{208}Pb+^{208}Pb collision at 0.3 GeV/u. The abscissa is the reduced rapidity defined by $y^{(0)} = y_{\mathrm{lab}}/y_{\mathrm{cm}} - 1$, where y_{lab} is the rapidity of particles in the laboratory reference, and y_{cm} is the rapidity of the center of mass of the collision system. The ordinate corresponds to the reduced transverse velocity $u_{\mathrm{t}}^{(0)} = p_{\mathrm{t}}/m\beta_{\mathrm{b}}\gamma_{\mathrm{b}}$, where p_{t} and m represent the transverse momentum and the mass of the particles, respectively. Here β_{b} and γ_{b} are the beam velocity and the corresponding Lorentz factor in laboratory. The curves corresponding to different angles in laboratory reference are plotted on top of the data. The MWDC array covers the range below $30°$, while the TPC mainly covers $\theta_{\mathrm{lab}} > 30°$. It is clear that since the target is placed in the space between the two TPC with a distance of 15 cm to the rear end of TPCs, the space at large angles with $\theta_{\mathrm{lab}} > 90°$ are also partly covered. From the phase space distribution of protons, it is also shown that in the vicinity of $30°$ both TPC and MWDC have the detection ability and hence this region is overlapped. It is shown that more than 90% of the phase space in center of mass can be covered, particularly for the symmetric systems because one can reflect the distribution with respect to $y^{(0)} = 0$ following the physical requirement.

Fig.8 shows the scattering plot of the momenta p *vs.* θ_{lab} for protons, tritium, π^+ and π^- in the reaction of ^{208}Pb+^{208}Pb at 0.3 GeV/u in laboratory reference system. The distribution only pass the filter of TPC and MWDC with a track length cut $L_{trk} > 30$ cm, while no conditions of the TOF hits are applied. Again, the wide angular acceptance of the tracking detectors are illustrated.

Fig.9 further presents the angular coverage of the tracking detector TPC and MWDC on $\theta - \phi$ plane for protons as an example. Particles with a track length shorter than 30 cm in the TPC have been cut. While the polar angle is well covered at $\theta_{\mathrm{lab}} < 100°$, there is obvious efficiency lose in azimuth. Namely in the vicinity of $\phi \approx 90°$ and $\phi \approx 270°$, both detectors lose the detection ability.

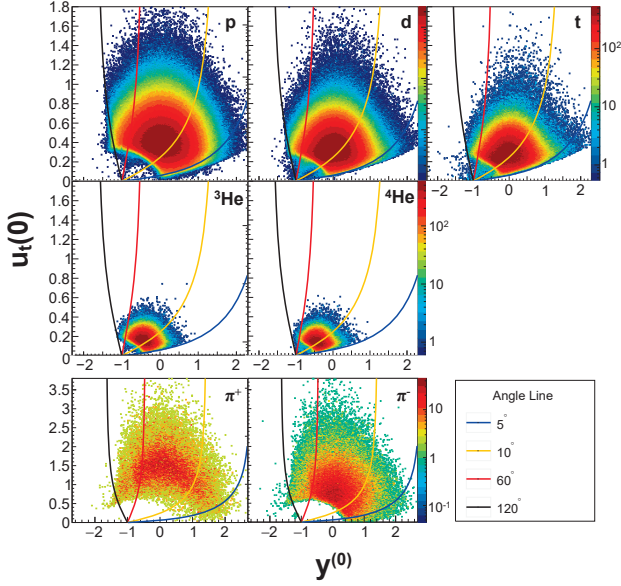FIG. 7. (Color online) The phase space distribution of various produced particles in the ^{208}Pb+^{208}Pb collision at 0.3 GeV/u.
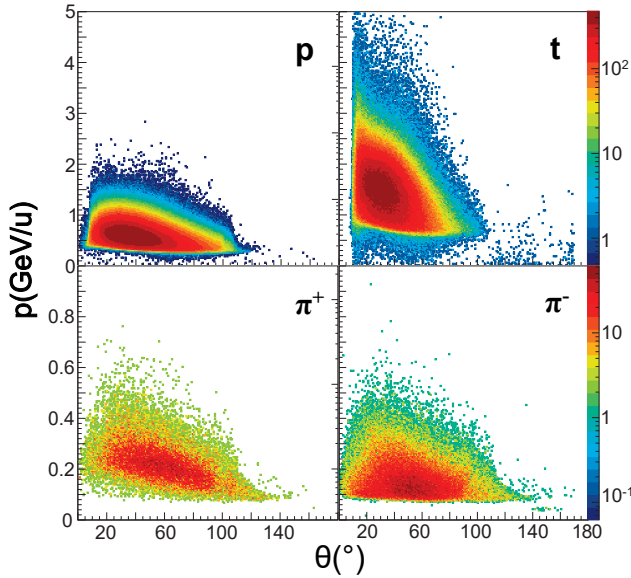

FIG. 8. (Color online) Correlation between the momentum p and polar angle θ_{lab} in laboratory for protons, tritium, π^+ and π^- in the reactions of ^{208}Pb+^{208}Pb at 0.3 GeV/u.

B. Particle identification

Since CEE has two tracking detectors, TPC and MWDC, and TOF detectors, both methods using $dE/dx - p/Q$ and $p - TOF$ can be applied, respectively. In the simulation studies, for the $dE/dx - p/Q$ correlation obtained by TPC and MWDC, the total energy loss dE is accumulated in each step when a particle is propagating in the sensitive volume of TPC or MWDC filled
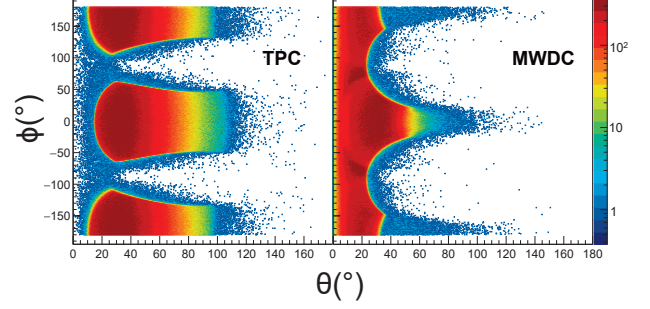

FIG. 9. (Color online) Angular coverage of proton by the tracking detectors TPC (a) and MWDC (b).

with the working gas of (90% Ar + 10% CO_2). When a complete cell is processed, the energy loss rate of dE/dx is calculated by summing the energy losses in all steps and smeared by a given variance. Since the distribution of dE/dx follows Landau formula showing divergence at large value, usually a high energy cut is applied to fill the histogram. The momentum p is obtained by fitting the hits generated by the ionization of the energetic particles in propagation. Tracking finding is not yet implemented, so the fitting is done directly to each individual track and a smearing is introduced directly according to the position resolution of the tracking detector. Fig. 10 presents the $dE/dx - p/Q$ for TPC and MWDC, respectively. It is shown that different isotopes of $Z = 1$ and $Z = 2$ can be well identified in TPC. While in MWDC, due to the total sampling times is only 18, corresponding to 18 layers of anode wire planes, the determination of the momentum is moderately degraded, although the tracking residue is controlled in 300 μm.
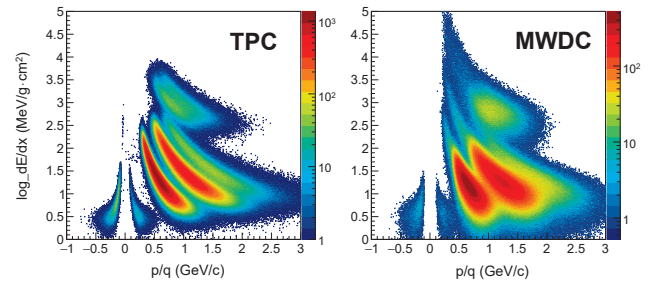

FIG. 10. (Color online) The predictions of particle identification in TPC and MWDC using the energy loss dE/dx as a function of magnetic rigidity p/q.

With increasing of p/q, the separation between neighbouring bands on the $dE/dx - p/q$ is reduced, particularly between pions and protons beyond 1 GeV/c. Thus, $p - $TOF correlation is applied to improve the PID ability. Once the track length L_{trk} is determined by the tracking detectors, the speed of the particle can be calculated and the mass m can be resolved at a given momentum p by

[72]

$$m = \frac{p}{c}\sqrt{\frac{c^2t^2}{L_{\text{trk}}^2} - 1} \qquad (8)$$

where c is the speed of light. This method can be applied for both configurations of TPC+iTOF and MWDC+eTOF, respectively. To achieve the intended performance, the timing resolutions of iTOF and eTOF are designed as 50 ps and 60 ps, respectively. Fig.11 presents the velocity of the particles as a function of the momentum p measured in TPC. It is shown that the pions and $Z = 1$ isotopes are well identified.
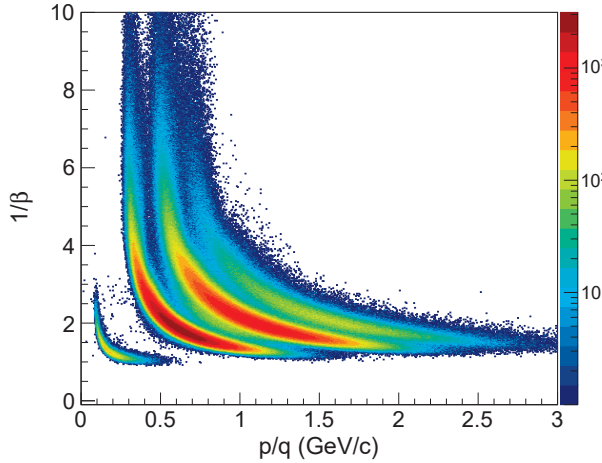

FIG. 11. (Color online) The change of charged particle flight velocity with momentum measured by iTOF

Fig.12(a) shows the mass and momentum correlation by combining the eTOF delivering the time of flight and MWDC providing the momentum information. The mass distribution is further plotted in Fig.12(b). It can be seen that at the beam energies of interest, the light charged particles with $Z = 1$ can be separated clearly, although a small distortion is occurred at the low momentum border due to the influence of the gap of the detectors, which is not corrected in the track length estimation.
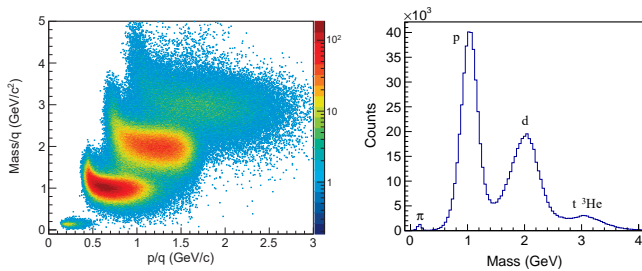

FIG. 12. (Color online) (a) Mass m and momentum p scattering plot obtained by eTOF and MWDC, (b) mass distribution spectrum.

The resolution of the momentum reconstruction of the

tracks in $\vec{B}$ field is determined by the hit position resolution and the track length L in the bending area, written as

$$(\frac{\sigma_p}{p})^2 = (\frac{720}{N+4}\frac{\sigma_{\text{xz}}p_{\text{xz}}}{0.3BL_{\text{trk}}^2}) + (\frac{0.0523}{\beta B\sqrt{L_{\text{trk}}X_0}\sin\theta}) + (\cot\theta\sigma_\theta)^2 \quad (9)$$

where B is the magnetic field strength and θ is the polar angle. N is the number of samplings, σ_{xz} and σ_θ are the hit position resolution in x-z plane perpendicular to the field $\vec{B}$ and the angular resolution, respectively. $X_0 = 1.2$ m is the radiation length. Given the hit position uncertainty of the tracks in the tracking detectors, the resolution of the momentum reconstruction can be investigated by fast simulations.

Fig.13 shows the resolution of the momentum reconstructed from the hit information collected from sensitive volume of TPC for 0.3 GeV/u ^{208}Pb+^{208}Pb at $b = 0$ fm. $\sigma_{\text{xz}} = 0.6$ mm and $\sigma_\theta = 0.5°$ are applied. It is shown that the typical resolution of $\pi^\pm$, proton and deuterium is about 5%. With the increase of momentum or in the forward angle region, the momentum resolution is gradually degraded, suggesting the necessity of using tracking detector array at forward angle for the dipole-type spectrometer. Namely, the MWDC array is designed for CEE. The degrades of the resolution at low momenta is mainly due to the loss of tracking efficiency because the tracks with low momentum leave very short length in the sensitive volume.

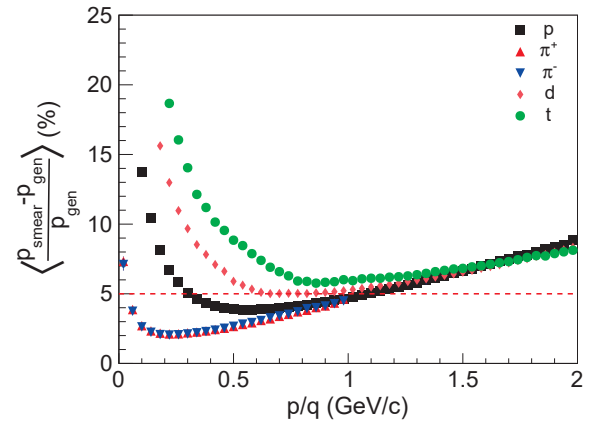FIG. 13. (Color online) Momentum resolution of TPC in fast simulation

C. Global trigger signal construction

In the beam experiment of the CEE, the construction of the global physical trigger signal has a twofold goals: 1) First, one has to select the collisions on the target and suppress the background events on the beam path and 2) It can provide trigger signals for the events at given

geometry, usually called as collision centrality. Similar scheme is usually adapted in the existing spectrometers, for instance, as by FOPI [73] and SAMURAI [74].
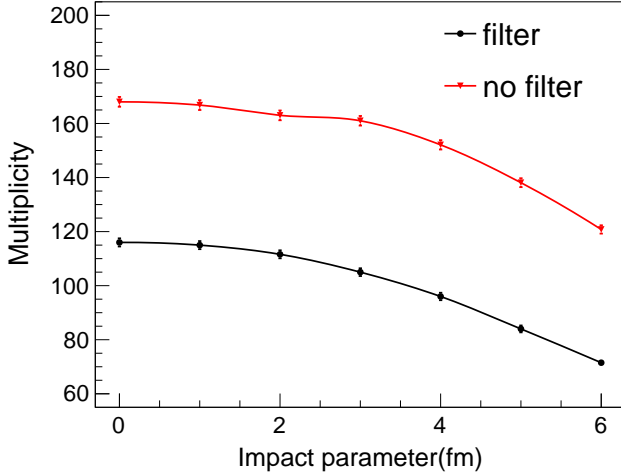

FIG. 14. (Color online) 0.5 GeV/u ^{208}Pb+^{208}Pb reaction system, under the collision parameter b=0,1,2,3,4,5,6fm, the multiplicity of charged particles changes with the collision parameters before and after passing through the detector. The red (black) curve is the data before (after) the detector filtering.

At CEE, the multiplicity of charged particles firing the fast detectors, including iTOF and eTOF, is employed to construct the global trigger because it can provide an approximate measure of the collision centrality. Figure 14 presents the multiplicity of charged particles as a function of the impact parameter b in the transport model simulations of the reactions ^{208}Pb+^{208}Pb at 0.5 GeV/u. The multiplicity distributions before (open) and after (solid) the filter of the iTOF and eTOF are presented. It can be clearly seen that the multiplicity of charged particles firing the iTOF and eTOF is anti correlated with b, giving certain ability to select the event centrality as the trigger signal of the CEE spectrometer.

IV. STUDY ON THE EOS OF NUCLEAR MATTER

In this section, we present the feasibility of studying the nuclear equation of state using several selected observables at CEE. In the HIC in the energy domain of hundreds of MeV/u, the nuclear matter can be compressed to approximately $2\rho_0$, where ρ_0 is the saturation density. In addition, due to the large stopping and large spatial-temporal volume, the sensitivity of the observable on nEOS is expected to be enhanced [75, 76]. Thus, it is of interest to check whether the information of EOS carried by various the observables is discernible at CEE.

A. light nuclear production

One of the physical goal of CEE is to measure systematically the production of ^{3}H and ^{3}He at the beam energies between 300 and 600 MeV/u. The motivation of this measurement is to understand the correlation between clustering and the isospin transport in HIC before arriving at a more stringent constraint on nuclear symmetry energy. It has been proposed that the yield ratio of ^{3}H/^{3}He in HIC in wide energy range is a sensitive probe of nuclear symmetry energy [77–84]. However, the origin of ^{3}H and ^{3}He are very complicated and the clustering process is reportedly correlated to the transport of isospin degree of freedom. Experimentally, in the energy regime of 1 GeV/u, a systematic data of the production of pions, protons and light clusters including ^{3}H and ^{3}He have been published by FOPI collaboration [17, 85], but in some other experiments, the ^{3}H $-^3$He puzzle has been reported [86, 87].

With the aim of measuring the ^{3}H/^{3}He ratio, the events generated by UrQMD model are analyzed in the fast simulation framework of CEEROOT. Fig.15 presents the ^{3}H/^{3}He ratio as a function of beam energy of ^{208}Pb+^{208}Pb system given different slope parameter of $E_{sym}(\rho)$, $\gamma = 0.5$ (soft) and 1 (stiff), respectively. The charged products are filtered by the tracking detectors. It is shown that the yield ratio ^{3}H/^{3}He exhibits certain sensitivity on $E_{sym}(\rho)$ and the difference between $\gamma = 0.5$ and 1 is kept after the detector filtering.
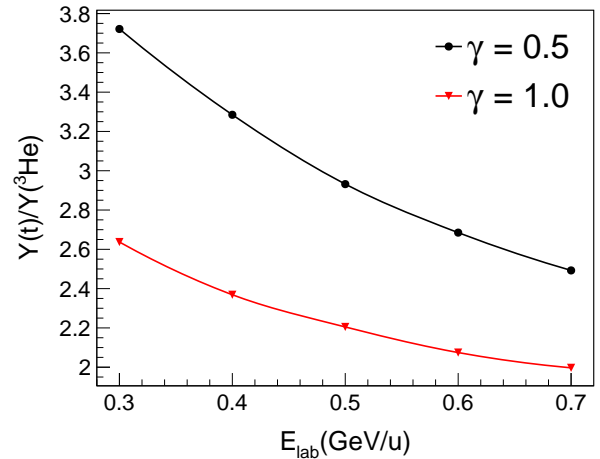

FIG. 15. (Color online) The ^{3}H/^{3}He yield ratio as a function of beam energy for reaction system ^{208}Pb+^{208}Pb at different symmetry energy parameters $\gamma = 0.5, 1.0$

In order to clarify whether the symmetry energy takes effect on the clustering process, one can further investigate the degree of clustering by looking at the ratio of the number of free protons to that of bounded in clusters produced in the HICs. In a general picture, the isospin dependent N-N cross sections, the nuclear symmetry po-

tential and the Coulomb interactions are convoluted in forming the clusters as well as the emission of free protons. Therefore, the yield of the free protons, in comparison to the the bounded protons, carries presumably the information of the nuclear symmetry energy $E_{\mathrm{sym}}(\rho)$, although the evolution of the system from a compression phase at early stage to the freeze-out stage is complicated and depends on the transport models.

Fig.16 presents the excitation function of the ratio of the free and bounded protons for the central collisions $^{208}\mathrm{Pb}+^{208}\mathrm{Pb}$ at 300 MeV/u using different $\gamma = 0.5$ and 1.0, respectively. The yield of bounded proton counts the charge of the light particles with $Z < 3$ in the final state of the reaction, including d, t, $^3\mathrm{He}$ and $^4\mathrm{He}$. The ratio increases gradually with the beam energy, indicating that the clustering is more favored at low beam energy. Moreover, it is shown that the degree of clustering, measured by the ratio $Y_p^{\mathrm{free}}/Y_p^{\mathrm{bound}}$, can differentiate the stiffness of $E_{\mathrm{sym}}(\rho)$. With a softer symmetry energy ($\gamma = 0.5$), more protons are found in the clusters.
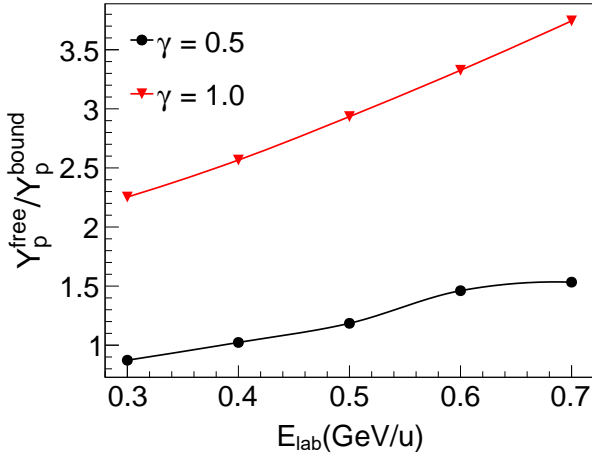

FIG. 16. (Color online) The ratio of free protons to that bounded in light clusters as a function of beam energy in $^{208}\mathrm{Pb}+^{208}\mathrm{Pb}$ reactions. Two parameters of $E_{\mathrm{sym}}(\rho)$, $\gamma = 0.5$ and 1.0 are compared.

B. Radial flow and EoS of nuclear matter

It has been realized since long time that the collective flow is an observable of great significance for studying the equation of state of nuclear matter under extreme conditions [88–94]. Depending on the collision geometry, the collective flow has different forms. In non central collisions, collective motion of HIC manifests itself in directional flow and elliptic flow, denoting the first and second order coefficient of the Fourier expansion of the azimuthal distribution of the final products, respectively [95]. In central collisions, the fireball produced in the collision experiences compression following by an expansion, forming the so-called radial flow [96]. It can be expected

that the size of radial flow depends on the compressibility of nuclear matter [84, 97]. Later, it is demonstrated by FOPI collaboration that the radial flow is sensitive to the incompressibility coefficient of nuclear matter [85]. In this subsection, the detection of radial flow with CEE is discussed.

The radial flow can be extracted from the transverse momentum spectra of the final particles at midrapidity in the central collisions. Two methods have been developed to obtain the expansion velocity β_r, one is to fit the p_t spectra using Siemens-Rasmussen formula [98], the other is to extract the dependence of the mean kinetic energy as a function of the mass of final products based on blast wave model [99–101]. In both methods, the thermal motion characterized by the temperature T and the expansion velocity β_r are included. Here it is attempted to study the radial flow by the Siemens-Rasmussen formula [98] written as:

$$\frac{1}{p_{\mathrm{t}}}\frac{d^2N}{dp_{\mathrm{t}}dy^0} = CEe^{-\gamma E/T}[(\gamma+\frac{T}{E})\frac{\sinh\alpha}{\alpha} - \frac{T}{E}\cosh\alpha] \quad (10)$$

where $\gamma = 1/\sqrt{1-\beta_r^2}$, $\alpha = \beta_r p\gamma/T$, E and p are the energy and momentum of the particle in the center of mass reference. The radial expansion velocity β_r, thermal freeze out temperature T and the constant C are the fitting parameters.

Fig.17 presents the feasibility of the radial flow measurement in central collisions of $^{208}\mathrm{Pb}+^{208}\mathrm{Pb}$ at CEE. Panel (a) presents the p_t spectra of proton, deuteron and triton. The low momentum parts are filtered by the acceptance cut and track length cut. The curves are the simultaneous fitting results using formula (10). It can be seen that the p_t spectra can be reproduced fairly well by Siemens-Rasmussen formula. In panel (b), the minimum χ^2 distribution is plotted on the $T - \beta_r$ plane. It can be seen that by simultaneous fitting, the two parameters can be determined rather well. While in individual fitting to the $Z = 1$ isotopes, the two parameters are correlated.
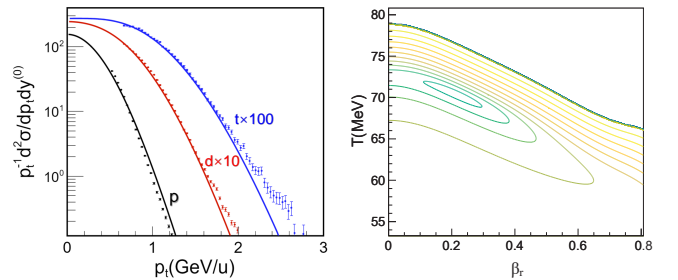

FIG. 17. (Color online) (a) The β_r and T are the fitting curves of the p_t spectrum and the model in $^{208}\mathrm{Pb}+^{208}\mathrm{Pb}$ at 0.4 GeV/u. The low transverse momentum part is eliminated in the fitting; (b) shows that χ^2/NDF is fitted as β_r and T.

Fig.18 presents the excitation function of β_r (a) and T (b) reconstructed from the simulations with $\kappa = 200$
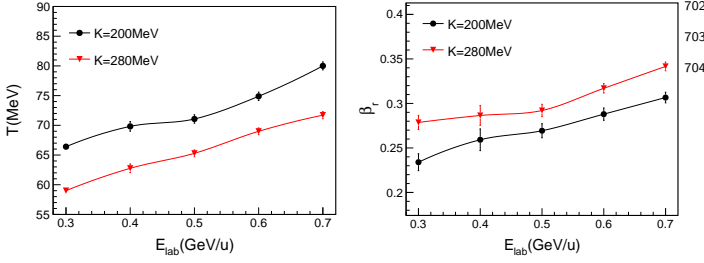
FIG. 18. (Color online) (a) It is shown that the thermal freeze out temperature T increases monotonically with the increase of beam energy in the energy range of 0.3 GeV/u to 0.7 GeV/u. (b) Shows radial flow β_r increases monotonically with the increase of beam energy in the energy range from 0.3 GeV/u to 0.7 GeV/u.

and 280 MeV, repsectively. The transport model simulation reveals that different incompressibility leads to different freeze-out temperature T and expansion velocity β_r. With a soft incompressibility constant, T is higher and β_r is lower, relatively, and *vise versa*. The difference is larger than 10% for most of the cases. It suggests that hard nuclear matter causes violent compression and expansion, while the soft nuclear matter tends to convert more kinetic energy to thermal energy in the procedure of the collision. It is also suggested that CEE has the ability for the studies of radial flow in the collisions of heavy system.

C. π^-/π^+ yield ratio and symmetry energy

The yield ratio of π^-/π^+ produced in HIC has been proposed as a sensitive probe of nuclear symmetry energy at supra-saturation densities [25, 79, 102–104]. In a transport picture, the pions are mainly produced by Δ resonance [33, 105]. From the isobaric model, the initial ratio $(\pi^-/\pi^+)_{\text{res}}=(5N^2 + NZ)/(5Z^2 + NZ) \approx (N/Z)^2_{\text{dense}}$, where N and Z are the number of neutrons and protons in the reaction participating region. Therefore, $(\pi^-/\pi^+)_{\text{res}}$ is a direct measure of the isospin asymmetry $(N/Z)_{\text{dense}}$, wihch is relatively higher than that of the system due to the isospin fractionation effect arising from $E_{\text{sym}}(\rho)$. In return, the yield ratio π^-/π^+ becomes a sensitive probe of $E_{\text{sym}}(\rho)$ [102]. In a statistic model [106], the ratio π^-/π^+ is related to the chemical potential of neutron and protons written as $\pi^-/\pi^+ \sim \exp[2(\mu_n - \mu_p)/T]$, where T is the system temperature, and $\mu_n - \mu_p$ is the difference between the chemical potentials of neutrons and protons, which depends on $E_{\text{sym}}(\rho)$ [107]. Circumstantial evidences of a soft $E_{\text{sym}}(\rho)$ has been found from the pion data of FOPI collaboration in accordance with the isospin fractionation picture [20]. However, the conclusion turns to be inconclusive because of the model dependence and the observable dependence, since the modeling of the pion

production transport, as well as clustering, is very complicated in transport model. For this direction, one can refer to [36, 37, 108].
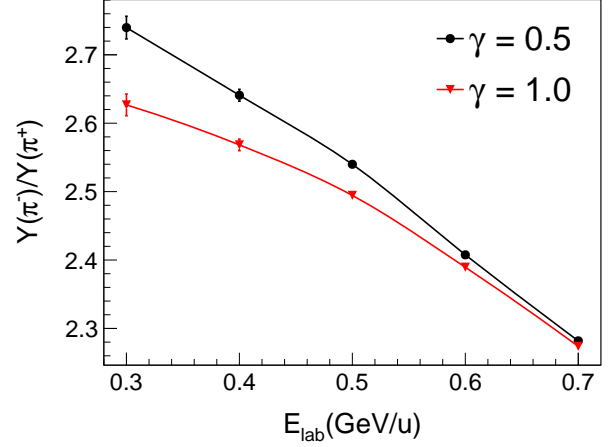

FIG. 19. (Color online) The excitation function of final π^-/π^+ yield ratio in $^{208}\text{Pb}+^{208}\text{Pb}$ reactions with different symmetry energy parameters $\gamma = 0.5$ and 1.0, respectively.

Therefore, pion physics is one of the focuses at CEE. In the current design of CEE, as shown in Fig.7(f),(g) in section III A, the whole phase space of pions on $u_t^{(0)} - y^{(0)}$ plane is well covered, although the efficiency on azimuth is lost near $\phi = 90°$ and $270°$ in laboratory. With the current efficiency, the final yield of π^-/π^+ in $^{208}\text{Pb}+^{208}\text{Pb}$ reactions at various beam energies are extracted and plotted in Fig.19 with $\gamma = 0.5$ and 1.0, respectively. It is shown that the ratio π^-/π^+ decreases with increasing of the beam energy. The difference between $\gamma = 0.5$ and 1 is also more pronounced at lower beam energy, in accordance with previous predictions for Au+Au systems [37]. This trend is due to the larger space-time volume of the fireball created in the collisions at lower energies [75]. It is suggested that at the favorable energy region of CEE, namely near 300 MeV/u , the stiffness of $E_{\text{sym}}(\rho)$ between $\gamma = 0.5$ and 1.0 can be discriminated if the systematic error can be controlled within 10%.

D. K_S^0 and incompressibility

Finally, let us discuss briefly the production and detection of kaons at CEE. Kaons are mainly produced in the supra-saturation density zone created in the early stage of the collisions, and the typical production channels are $B + B \rightarrow B + Y + K$, $\pi + B \rightarrow Y + K$. Kaon production is of interest in this energy region as a very clean probe to nuclear EOS because it experiences much less rescattering process in comparison to that of nucleons or pions. Since long time it has been pointed out that the yield of kaons is an effective probe for EoS of supra-

saturation density nuclear matter [109]. KaoS collaboration from GSI measured the yield of K^+ in C+C and Au+Au systems from 800 MeV/u to 1.6 GeV/u. Within the transport model framework, the yield ratio of K^+ in the two systems favors a soft nuclear matter [110, 111]. Compared to charged Kaons, the neutral kaon K^0 is not affected by Coulomb interactions, so the production of K^0 carries the information of the high-density medium where it is produced. The yields of these neutral strange particles were studied in detail on the SIS, BEVALAC and AGS [68, 112, 113].

Since the HIRFL-CSR can provide proton beam of the maximum energy 2.8 GeV and carbon beam of the maximum energy 1.2 GeV, it is also possible to conduct kaon experiments at CEE. Since the identification of K^+ may suffer from the heavy background caused by protons and pions, it is of our interest as the first step to measure the neutral K^0 decaying to π^+ and π^-, which are thus easier to be detected. Fig.20 shows the invariant mass spectrum of π^+ and π^- in p+Ni system at $\kappa = 200$ MeV. It is shown that, after the background are subtracted by mixing event method, a peak at K^0 mass is evidently seen. Totally 1 M central collision events are simulated and about 200 K^0_s are reconstructed. Worth mentioning, the background is not fully removed and there is an enhancement at low mass end, this is not due to the detector filtering, but possibly due to the residue baryon-baryon correlation since the majority of pions are produced via Δ resonances. Compared to the Monte-Carlo truth tracks, the reconstruction efficiency of K^0 is about 35%.

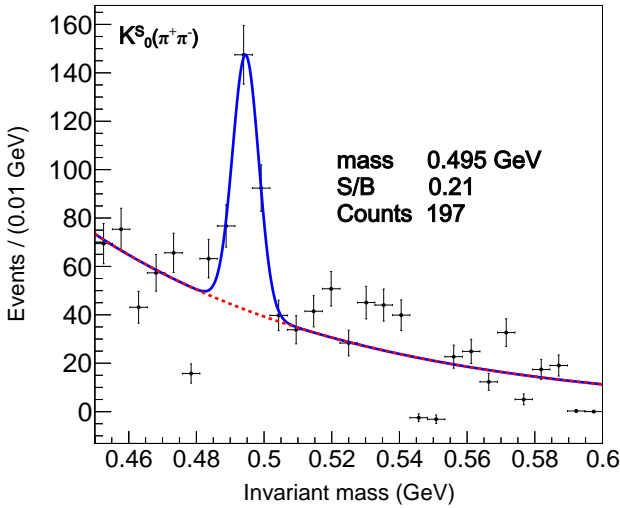
FIG. 20. (Color online) K^0_S invariant mass spectrum of p+Ni system at K=200 MeV

Fig.21 shows the yield of the reconstructed K^0 (mainly K^0_s) as a function of system size with two different incompressibility coefficients $\kappa = 200$ and 280 MeV, respectively. The yield of K^0 increases with the mass of

the system, and exhibits significant dependence on the incompressibility κ of the nuclear matter. As long as the systematic uncertainty can be controlled within 10%, the production of neutral Kaon K^0 can also be used as a probe of the nuclear equation of state, supporting one of the physical programs of CEE.
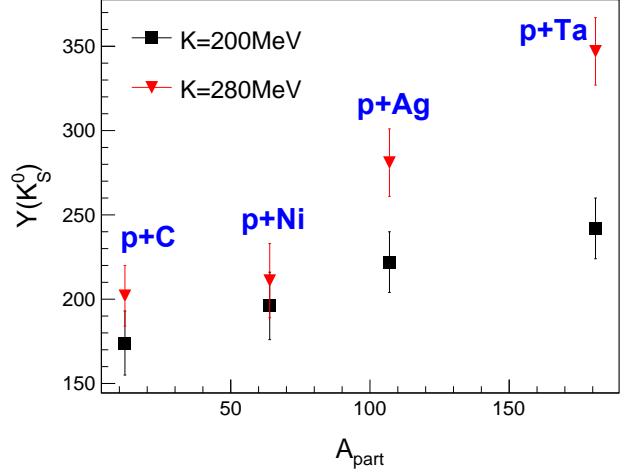

FIG. 21. (Color online) Variation of K^0_S yield in p+C, p+Ni, p+Ag and p+Ta reactions at beam energy of 2.8 GeV with two incompressibility $\kappa = 200$ and 280 MeV, respectively.

V. CONCLUSION

The conceptual design of CEE are briefly described. The expected performance is studied based on the Geant 4 simulations using UrQMD as the event generator. The main part of the detector system is a large-acceptance magnetic dipole housing the tracking detectors and the surrounding TOF detecotrs. TPC and MWDC are employed to cover the midrapidity and forward rapidity region for tracking, respectively. TOF detectors, including iTOF and eTOF, provide the main trigger signals constructed based on advanced FPGA technology. In the framework of CEEROOT, built *ad hoc* for the researches and developments ($R\&D$) of CEE, we have discussed the feasibility of the studies of nuclear equation of state through various observables, including the production of light clusters, $^3H/^3He$ yield ratio, radial flow, pion ratio and near-threshold Kaon production. The results of the simulations suggest that the aforementioned probes can be measured with CEE, giving the opportunity to the studies of properties of dense nuclear matter in the HIRFL-CSR energy regime.

DECLARATION OF COMPETING INTEREST

The authors declare that they have no known competing financial interests or personal relationships that

could have appeared to influence the work reported in this paper.

[1] I. Arsene et al. Quark–gluon plasma and color glass condensate at rhic? the perspective from the brahms experiment. *Nuclear Physics A*, 757(1):1–27, 2005. First Three Years of Operation of RHIC.

[2] B.B. Back et al. The phobos perspective on discoveries at rhic. *Nuclear Physics A*, 757(1):28–101, 2005. First Three Years of Operation of RHIC.

[3] B.M. Peter et al. The quest for the quark-gluon plasma. *Nature*, 448(7151):302–309, 2007.

[4] X.F. Luo et al. Search for the qcd critical point with fluctuations of conserved quantities in relativistic heavy-ion collisions at rhic : An overview. *Nuclear Science and Techniques*, 28(8):40, 2017.

[5] M.M. Aggarwal et al. Higher moments of net proton multiplicity distributions at rhic. *Phys. Rev. Lett.*, 105:022302, Jul 2010.

[6] L. Adamczyk et al. Bulk properties of the medium produced in relativistic heavy-ion collisions from the beam energy scan program. *Phys. Rev. C*, 96:044904, Oct 2017.

[7] X.F. Luo et al. Energy dependence of moments of net-proton and net-charge multiplicity distributions at star, 2015.

[8] X.F. Luo. Exploring the qcd phase structure with beam energy scan in heavy-ion collisions. *Nuclear Physics A*, 956:75–82, 2016. The XXV International Conference on Ultrarelativistic Nucleus-Nucleus Collisions: Quark Matter 2015.

[9] M.S. Abdallah et al. Cumulants and correlation functions of net-proton, proton, and antiproton multiplicity distributions in Au + Au collisions at energies available at the bnl relativistic heavy ion collider. *Phys. Rev. C*, 104:024902, Aug 2021.

[10] Stephanov M. A. Non-gaussian fluctuations near the qcd critical point. *Phys. Rev. Lett.*, 102:032301, Jan 2009.

[11] Stephanov M. A. Sign of kurtosis near the qcd critical point. *Phys. Rev. Lett.*, 107:052301, Jul 2011.

[12] K. Masakiyo and X.F Luo. Properties and uses of factorial cumulants in relativistic heavy-ion collisions. *Phys. Rev. C*, 96:024910, Aug 2017.

[13] J. Adam et al. Nonmonotonic energy dependence of net-proton number fluctuations. *Phys. Rev. Lett.*, 126:092301, Mar 2021.

[14] L. Adamczyk et al. Beam energy dependence of moments of the net-charge multiplicity distributions in Au + Au collisions at rhic. *Phys. Rev. Lett.*, 113:092301, Aug 2014.

[15] L. Adamczyk et al. Collision energy dependence of moments of net-kaon multiplicity distributions at rhic. *Physics Letters B*, 785:551–560, 2018.

[16] B.A. Li et al. Topical issue on nuclear symmetry energy. *The European Physical Journal, A. Hadrons and Nuclei*, 50(2), 2014.

[17] W. Reisdorf et al. Systematics of azimuthal asymmetries in heavy ion collisions in the 1a gev regime. *Nuclear Physics A*, 876:1–60, 2012.

[18] P. Hillmann et al. Directed, elliptic and triangular flow of protons in au+au reactions at 1.23 a gev: a theoretical analysis of the recent hades data. *Journal of Physics G: Nuclear and Particle Physics*, 45(8):085101, jun 2018.

[19] B.A. Li et al. Equation of state of asymmetric nuclear matter and collisions of neutron-rich nuclei. *Phys. Rev. Lett.*, 78:1644–1647, Mar 1997.

[20] H.S. Xu et al. Isospin fractionation in nuclear multifragmentation. *Phys. Rev. Lett.*, 85:716–719, Jul 2000.

[21] W.P. Tan et al. Fragment isotope distributions and the isospin dependent equation of state. *Phys. Rev. C*, 64:051901, Sep 2001.

[22] M.B. Tsang et al. Isotopic scaling in nuclear reactions. *Phys. Rev. Lett.*, 86:5023–5026, May 2001.

[23] B.A. Li et al. Proton differential elliptic flow and the isospin dependence of the nuclear equation of state. *Phys. Rev. C*, 64:054604, Oct 2001.

[24] B.A. Li. Neutron-proton differential flow as a probe of isospin-dependence of the nuclear equation of state. *Phys. Rev. Lett.*, 85:4221–4224, Nov 2000.

[25] Z.G. Xiao et al. Probing nuclear symmetry energy at high densities using pion, kaon, eta and photon productions in heavy-ion collisions. *The European Physical Journal A*, 50:37, February 2014.

[26] B.A. Li. Isospin dependence of the π^-/π^+ ratio and density dependence of the nuclear symmetry energy. *Phys. Rev. C*, 67:017601, Jan 2003.

[27] D. Adhikari et al. Accurate determination of the neutron skin thickness of ^{208}Pb through parity-violation in electron scattering. *Phys. Rev. Lett.*, 126:172502, Apr 2021.

[28] T.R. Brendan et al. Implications of prex-2 on the equation of state of neutron-rich matter. *Phys. Rev. Lett.*, 126:172503, Apr 2021.

[29] Y. Zhang et al. Long-time drift of the isospin degree of freedom in heavy ion collisions. *Phys. Rev. C*, 95:041602, Apr 2017.

[30] Y.J. Wang et al. Observing the ping-pong modality of the isospin degree of freedom in cluster emission from heavy-ion reactions. *Phys. Rev. C*, 107:L041601, Apr 2023.

[31] J. Estee et al. Probing the symmetry energy with the spectral pion ratio. *Phys. Rev. Lett.*, 126:162701, Apr 2021.

[32] Y. Zhou et al. Equation of state of dense matter in the multimessenger era. *Phys. Rev. D*, 99:121301, Jun 2019.

[33] Y.Y. Liu et al. Insights into the pion production mechanism and the symmetry energy at high density. *Phys.*

Rev. C, 103:014616, Jan 2021.

[34] B.A. Li et al. Progress in constraining nuclear symmetry energy using neutron star observables since gw170817. *Universe*, 7(6), 2021.

[35] B.A. Li. Towards understanding astrophysical effects of nuclear symmetry energy. *The European Physical Journal A*, 55:117, July 2019.

[36] W. Reisdorf et al. Systematics of pion emission in heavy ion collisions in the 1a gev regime. *Nuclear Physics A*, 781(3):459–508, 2007.

[37] Z.G Xiao et al. Circumstantial evidence for a soft nuclear symmetry energy at suprasaturation densities. *Phys. Rev. Lett.*, 102:062502, Feb 2009.

[38] W.J. Xie et al. Symmetry energy and pion production in the boltzmann–langevin approach. *Physics Letters B*, 718(4):1510–1514, 2013.

[39] P. Russotto et al. Symmetry energy from elliptic flow in 197au+197au. *Physics Letters B*, 697(5):471–476, 2011.

[40] X.F Luo et al. Properties of qcd matter at high baryon density. 2022.

[41] L.M. Lyu et al. Conceptual design of the hirfl-csr external-target experiment. *Science China Physics, Mechanics & Astronomy*, 60:012021, November 2016.

[42] Y. J. Yuan et al. Present status of hirfl complex in lanzhou. *Journal of Physics: Conference Series*, 1401(1):012003, jan 2020.

[43] Z.Y. Sun et al. Huizhou accelerator complex facility and its future development. *SCIENTIA SINICA Physica Mechanica Astronomica*, 50:112006, 11 2020.

[44] Qingfeng Li, Caiwan Shen, Chenchen Guo, Yongjia Wang, Zhuxia Li, J. Lukasik, and W. Trautmann. Nonequilibrium dynamics in heavy-ion collisions at low energies available at the GSI Schwerionen Synchrotron. *Phys. Rev. C*, 83:044617, 2011.

[45] Yongjia Wang, Qingfeng Li, Yvonne Leifels, and Arnaud Le Fèvre. Study of the nuclear symmetry energy from the rapidity-dependent elliptic flow in heavy-ion collisions around 1 GeV/nucleon regime. *Phys. Lett. B*, 802:135249, 2020.

[46] Y.J Wang et al. Application of microscopic transport model in the study of nuclear equation of state from heavy ion collisions at intermediate energies. *Frontiers of Physics*, 15:44302, May 2020.

[47] https://fairroot.gsi.de./.

[48] Li He et al. Simulation of momentum resolution of the cee-tpc in hirfl. *Nuclear Techniques*, 39(070401), May 2016.

[49] X. Wang et al. Cee inner tof prototype design and preliminary test results. *Journal of Instrumentation*, 17(09):P09023, sep 2022.

[50] B. Wang et al. The cee-etof wall constructed with new sealed mrpc. *Journal of Instrumentation*, 15(08):C08022, aug 2020.

[51] S.H. Zhu et al. Prototype design of readout electronics for zero degree calorimeter in the hirfl-csr external-target experiment. *Journal of Instrumentation*, 16(08):P08014, aug 2021.

[52] D. Hu et al. A t0/trigger detector for the external target experiment at csr. *Journal of Instrumentation*, 12(06):C06010, jun 2017.

[53] D.D. Hu et al. Extensive beam test study of prototype mrpcs for the t0 detector at the csr external-target experiment. *The European Physical Journal C*, 80:282, March 2020.

[54] H.L. Wang et al. Design and tests of the prototype beam monitor of the csr external target experiment. *Nuclear Science and Techniques*, 33:36, march 2022.

[55] J. Liu et al. Design and preliminary characterization of a novel silicon charge sensor for the gaseous beam monitor at the csr external-target experiment. *Nuclear Instruments and Methods in Physics Research Section A: Accelerators, Spectrometers, Detectors and Associated Equipment*, 1047:167786, 2023.

[56] J. Adolfsson et al. Sampa chip: the new 32 channels asic for the alice tpc and mch upgrades. *Journal of Instrumentation*, 12(04):C04008, apr 2017.

[57] J.Y Yuan et al. Development of multichannel readout electronics prototype system for tpc detector of csr external-target experiment. *Nuclear Instruments and Methods in Physics Research Section A: Accelerators, Spectrometers, Detectors and Associated Equipment*, 1052:168281, 2023.

[58] F. Anghinolfi et al. Nino, an ultra-fast, low-power, front-end amplifier discriminator for the time-of-flight detector in alice experiment. In *2003 IEEE Nuclear Science Symposium. Conference Record (IEEE Cat. No.03CH37515)*, volume 1, pages 375–379 Vol.1, 2003.

[59] J.M. Lu et al. Readout electronics prototype of tof detectors in cee of hirfl. *IEEE Transactions on Nuclear Science*, 68(8):1976–1983, 2021.

[60] S.A. Bass et al. Microscopic models for ultrarelativistic heavy ion collisions. *Progress in Particle and Nuclear Physics*, 41:255–369, 1998.

[61] M Bleicher et al. Relativistic hadron-hadron collisions in the ultra-relativistic quantum molecular dynamics model. *Journal of Physics G: Nuclear and Particle Physics*, 25(9):1859, sep 1999.

[62] Yongjia Wang, Chenchen Guo, Qingfeng Li, Hongfei Zhang, Zhuxia Li, and W. Trautmann. Collective flows of light particles in the Au+Au collisions at intermediate energies. *Phys. Rev. C*, 89(3):034606, 2014.

[63] Yongjia Wang, Chenchen Guo, Qingfeng Li, Hongfei Zhang, Y. Leifels, and W. Trautmann. Constraining the high-density nuclear symmetry energy with the transverse-momentum dependent elliptic flow. *Phys. Rev. C*, 89(4):044603, 2014.

[64] Qing-feng Li, Zhu-xia Li, Sven Soff, Marcus Bleicher, and Horst Stoecker. Medium modifications of the nucleon-nucleon elastic cross section in neutron-rich intermediate energy HICs. *J. Phys. G*, 32:407–416, 2006.

[65] Pengcheng Li, Yongjia Wang, Qingfeng Li, Chenchen Guo, and Hongfei Zhang. Effects of the in-medium nucleon-nucleon cross section on collective flow and nuclear stopping in heavy-ion collisions in the Fermi-energy domain. *Phys. Rev. C*, 97(4):044620, 2018.

[66] Pengcheng Li, Yongjia Wang, Qingfeng Li, and Hongfei Zhang. Accessing the in-medium effects on nucleon-nucleon elastic cross section with collective flows and nuclear stopping. *Phys. Lett. B*, 828:137019, 2022.

[67] Yingxun Zhang, Zhuxia Li, Chengshuang Zhou, and M. B. Tsang. Effect of isospin dependent cluster recognition on the observables in heavy ion collisions. *Phys. Rev. C*, 85:051602, 2012.

[68] YuShan Du, YongJia Wang, QingFeng Li, and Ling Liu. The effect of Lorentz-like force on collective flows of K^+ in Au+Au collisions at 1.5 GeV/nucleon. *Sci. China Phys. Mech. Astron.*, 61(6):062011, 2018.

[69] Yangyang Liu, Yongjia Wang, Qingfeng Li, and Ling Liu. Collective flows of pions in Au+Au collisions at energies 1.0 and 1.5 GeV/nucleon. *Phys. Rev. C*, 97(3):034602, 2018.

[70] Yangyang Liu, Yongjia Wang, Ying Cui, Chen-Jun Xia, Zhuxia Li, Yongjing Chen, Qingfeng Li, and Yingxun Zhang. Insights into the pion production mechanism and the symmetry energy at high density. *Phys. Rev. C*, 103(1):014616, 2021.

[71] Y.X Zhang et al. Progress of quantum molecular dynamics model and its applications in heavy ion collisions. *Frontiers of Physics*, 15(54301), May 2020.

[72] W. Klempt. Review of particle identification by time of flight techniques. *Nuclear Instruments and Methods in Physics Research Section A: Accelerators, Spectrometers, Detectors and Associated Equipment*, 433(1):542–553, 1999.

[73] Y. Kim. *Study of nuclear stopping in isospin asymmetric nuclear collisions at 0.4 and 1.5 GeV*. Dr. Seoul, Korea, Univ., 2004. Seoul, Korea, Univ. , Diss., 2004.

[74] T. Kobayashi et al. Samurai spectrometer for ri beam experiments. *Nuclear Instruments and Methods in Physics Research Section B: Beam Interactions with Materials and Atoms*, 317:294–304, 2013. XVIth International Conference on ElectroMagnetic Isotope Separators and Techniques Related to their Applications, December 2–7, 2012 at Matsue, Japan.

[75] M. Zhang et al. Systematic study of the π^-/π^+ ratio in heavy-ion collisions with the same neutron/proton ratio but different masses. *Phys. Rev. C*, 80:034616, Sep 2009.

[76] F. Fen et al. Nuclear stopping and compression in heavy-ion collisions at intermediate energies. *Physics Letters B*, 666(4):359–363, 2008.

[77] L.W. Chen et al. Effects of symmetry energy on two-nucleon correlation functions in heavy-ion collisions induced by neutron-rich nuclei. *Phys. Rev. Lett.*, 90:162701, Apr 2003.

[78] L.W. Chen et al. Effects of momentum-dependent nuclear potential on two-nucleon correlation functions and light cluster production in intermediate energy heavy-ion collisions. *Phys. Rev. C*, 69:054606, May 2004.

[79] Q.F. Li et al. Probing the density dependence of the symmetry potential at low and high densities. *Phys. Rev. C*, 72:034613, Sep 2005.

[80] Y.X. Zhang et al. Probing the density dependence of the symmetry potential with peripheral heavy-ion collisions. *Phys. Rev. C*, 71:024604, Feb 2005.

[81] Y.J. Wang et al. 3h/3he ratio as a probe of the nuclear symmetry energy at sub-saturation densities. *The European Physical Journal A*, 51:37, 2015.

[82] C.C. Guo et al. Influence of the symmetry energy on the balance energy of the directed flow. *Science China Physics, Mechanics and Astronomy*, 55:252–259, 2012.

[83] K. Hagel et al. Light particle probes of expansion and temperature evolution: Coalescence model analyses of heavy ion collisions at 47aMeV. *Phys. Rev. C*, 62:034607, Aug 2000.

[84] L.W. Chen et al. Light clusters production as a probe to nuclear symmetry energy. *Phys. Rev. C*, 68:017601, Jul 2003.

[85] W. Reisdorf et al. Systematics of central heavy ion collisions in the 1a gev regime. *Nuclear Physics A*, 848(3):366–427, 2010.

[86] J.F. Dempsey et al. Isospin dependence of intermediate mass fragment production in heavy-ion collisions at e/a=55 mev. *Phys. Rev. C*, 54:1710–1719, Oct 1996.

[87] M. Veselsky et al. Isospin dependence of isobaric ratio y(3(h)/y(3he) and its relation to temperature. *Physics Letters B*, 497(1):1–7, 2001.

[88] J.Y. Ollitrault. Flow systematics from sis to sps energies. *Nuclear Physics A*, 638(1):195c–206c, 1998. Quark Matter '97.

[89] W. Bauer et al. Large radial flow in nucleus-nucleus collisions. *Phys. Rev. C*, 47:R1838–R1841, May 1993.

[90] G. Poggi et al. Evidence for collective expansion in light-particle emission following au+au collisions at 100, 150 and 250 a·mev. *Nuclear Physics A*, 586(4):755–776, 1995.

[91] W. Reisdorf et al. Nuclear stopping from 0.09a to 1.93a GeV and its correlation to flow. *Phys. Rev. Lett.*, 92:232301, Jun 2004.

[92] G. Stoicea et al. Azimuthal dependence of collective expansion for symmetric heavy-ion collisions. *Phys. Rev. Lett.*, 92:072303, Feb 2004.

[93] J. Stachel. Tests of thermalization in relativistic nucleus-nucleus collisions. *Nuclear Physics A*, 610:509–522, 1996. Quark Matter '96.

[94] B.A. Li et al. Pion flow and antiflow in relativistic heavy-ion collisions. *Phys. Rev. C*, 53:R22–R24, Jan 1996.

[95] J.Y. Ollitrault. Determination of the reaction plane in ultrarelativistic nuclear collisions. *Phys. Rev. D*, 48:1132–1139, Aug 1993.

[96] J.P. Alard et al. Midrapidity source of intermediate-mass fragments in highly central collisions of au + au at 150a mev. *Phys. Rev. Lett.*, 69:889–892, Aug 1992.

[97] Ch. Hartnack et al. Transverse flow of nuclear matter in collisions of heavy nuclei atintermediate energies. *Physics Letters B*, 506(3):261–266, 2001.

[98] P.J. Siemens et al. Evidence for a blast wave from compressed nuclear matter. *Phys. Rev. Lett.*, 42:880–883, Apr 1979.

[99] H.A. Gustafsson et al. Collective flow observed in relativistic nuclear collisions. *Phys. Rev. Lett.*, 52:1590–1593, Apr 1984.

[100] M.A. Lisa et al. Radial flow in Au + Au collisions at $E = (0.25-1.15)A$GeV. *Phys. Rev. Lett.*, 75:2662–2665, Oct 1995.

[101] S. Wang et al. In-plane retardation of collective expansion in Au + Au collisions. *Phys. Rev. Lett.*, 76:3911–3914, May 1996.

[102] B.A. Li et al. Near-threshold pion production with radioactive beams. *Phys. Rev. C*, 71:014608, Jan 2005.

[103] B. Hong et al. Charged pion production in $^{96}_{44}$Ru $+ ^{96}_{44}$Ru collisions at $400a$ and $1528a$ MeV. *Phys. Rev. C*, 71:034902, Mar 2005.

[104] M.D. Cozma. Neutron–proton elliptic flow difference as a probe for the high density dependence of the symmetry energy. *Physics Letters B*, 700(2):139–144, 2011.

[105] R. Stock. Particle production in high energy nucleus-nucleus collisions. *Physics Reports*, 135(5):259–315, 1986.

[106] A. Bonasera et al. Isospin effects on pion production by heavy ions. *Physics Letters B*, 195(4):521–523, 1987.

[107] B.A. Li. Probing the high density behavior of the nuclear symmetry energy with high energy heavy-ion collisions. *Phys. Rev. Lett.*, 88:192701, Apr 2002.

[108] Z.G. Xiao et al. Isospin fractionation, isospin relaxation and asymmetric nuclear equation of state. *SCIENTIA SINICA Physica, Mechanica & Astronomica*, 41(4):439–445, 2011.

[109] J. Aichelin et al. Subthreshold kaon production as a probe of the nuclear equation of state. *Phys. Rev. Lett.* 55:2661–2663, Dec 1985.

[110] C. Sturm et al. Evidence for a soft nuclear equation-of-state from kaon production in heavy-ion collisions. *Phys. Rev. Lett.*, 86:39–42, Jan 2001.

[111] Ch. Hartnack et al. Hadronic matter is soft. *Phys. Rev. Lett.*, 96:012302, Jan 2006.

[112] P. Crochet et al. Sideward flow of k+ mesons in ru+ru and ni+ni reactions near threshold. *Physics Letters B*, 486(1):6–12, 2000.

[113] S. Albergo et al. Λ spectra in $11.6\,A\,GeV/c$ au-au collisions. *Phys. Rev. Lett.*, 88:062301, Jan 2002.